Kumar *et al. Energy Mater.* **2025**, *5*, 500109
DOI: 10.20517/energymater.2025.22

Energy Materials

Article

Open Access

Check for updates

Improved thermoelectric performance by grain connectivity in bismuth antimony telluride composite with metallic high-entropy alloy nanoparticles

Anil Kumar[1,#], Saurabh Thoravat[1,#], Jae Hyun Yun[1,#], Rahmatul Hidayati[1], Junyoung Park[2], Hyungyu Jin[2], Jin Hee Kim[1,*], Jong-Soo Rhyee[1,*]

[1]Department of Applied Physics and Institute of Natural Sciences, Kyung Hee University, Yongin 17104, Republic of Korea.
[2]Department of Mechanical Engineering, Pohang University of Science and Technology, Pohang 37673, Republic of Korea.
[#]Authors contributed equally.

[*]**Correspondence to:** Dr. Jin Hee Kim and Prof. Jong-Soo Rhyee, Department of Applied Physics and Institute of Natural Sciences, Kyung Hee University, Deogyeong-daero 1732, Yongin 17104, Republic of Korea. E-mail: jinheekim@khu.ac.kr; jsrhyee@khu.ac.kr

How to cite this article: Kumar, A.; Thoravat, S.; Yun, J. H.; Hidayati, R.; Park, J.; Jin, H.; Kim, J. H.; Rhyee, J. S. Improved thermoelectric performance by grain connectivity in bismuth antimony telluride composite with metallic high-entropy alloy nanoparticles. *Energy Mater.* **2025**, *5*, 500109. https://dx.doi.org/10.20517/energymater.2025.22

Received: 4 Mar 2025 **First Decision:** 6 Apr 2025 **Revised:** 16 Apr 2025 **Accepted:** 23 Apr 2025 **Published:** 19 May 2025

Academic Editor: Sen Xin **Copy Editor:** Ping Zhang **Production Editor:** Ping Zhang

Abstract

We investigated the anisotropic thermoelectric properties of $Bi_{0.4}Sb_{1.6}Te_3$ (BST) composites with heavy metallic high-entropy alloy $TaNb_2HfZrTi$ (HEA_x) (x = 0, 0.1, 0.5, and 1.0 vol%), synthesized by ball-milling, mixing, and hot-press sintering method. The HEA additions below 1.0 vol% in the BST+HEA_x samples do not contribute to the change of Seebeck coefficients, carrier concentrations, and Fermi energies. Besides, electrical conductivity in the parallel (Pa) direction to the press direction was significantly enhanced due to an increased carrier mean free path (λ_e) from 10.4 nm (x = 0) to 13.6 nm (x = 0.5). This enhanced λ_e is attributed to metallic HEA nanoparticles that improve electrical grain connectivity, particularly in the Pa-direction. The lattice thermal conductivities in the Pa-direction of the BST+HEA_x samples decreased at x = 0.1 vol% by significant phonon scattering, followed by an increase at higher HEA concentrations (0.5 vol% to 1.0 vol%), which is consistent with the values of the phonon mean free path. The phonon mean free path and lattice thermal conductivity of the composites indicate the synergistic competition between the phonon scattering and the grain connectivity in the Pa-direction. As a result, the thermoelectric figure of merit in the Pa-direction improved from 1.09 (x = 0) to 1.33 (x = 0.1 vol%) at 350 K. These findings suggest that incorporating heavy metallic HEA nanoparticles is a promising strategy to improve the performance of the anisotropic thermoelectric materials and other systems sensitive to grain connectivity.

Keywords: Bismuth antimony telluride, high-entropy alloy, grain connectivity, nanoparticles, mean free path, thermoelectrics

INTRODUCTION

Thermoelectric (TE) devices, which can directly enable waste heat recovery or eco-friendly solid-state cooling through the Seebeck effect and Peltier effect, respectively, have a wide range of interesting application fields. These include thermoelectric generators (TEGs), thermoelectric cooling devices, wearable TE devices, power systems for the Internet of Things (IoT), medical devices requiring sensitive temperature control, radioisotope thermoelectric generators (RTGs), battery thermal management systems for electric vehicles, and more[1-3]. Despite their advantages, such as direct energy conversion between heat and electricity, absence of moving parts, scalability, portability, eco-friendly operation, and low-grade heat recovery, the use of TE devices is limited in certain applications due to their relatively low energy conversion efficiency compared to other electricity generation or cooling systems[1,2,4]. Therefore, improving the thermoelectric performance of TE devices is essential to expand their range of applications.

The energy conversion efficiency of a TE device strongly depends on the dimensionless figure of merit (ZT) of the p- and n-type TE materials, defined as $ZT = S^2\sigma T/\kappa_{total}$, where S is the Seebeck coefficient, σ is the electrical conductivity, T is the absolute temperature and κ_{total} is the total thermal conductivity. Since these parameters are strongly interrelated, careful control of the material properties is required to enhance TE performance[1,2,4]. Various approaches can improve materials' TE performance, such as optimizing carrier concentration, reducing lattice thermal conductivity (κ_L), manipulating the band structure, employing low-dimensional structures, low-energy electron filtering, introducing defects, and leveraging resonant levels[2,5].

Bismuth tellurides are among the most well-known thermoelectric materials, exhibiting high performance near room temperature[1,4,6,7]. Their high ZT values have been achieved through various innovative approaches for the p-type bismuth antimony tellurides such as the hot-deformed $Bi_{0.3}Sb_{1.7}Te_3$ (1.3 at 380 K)[8], Te-excess $Bi_{0.4}Sb_{1.6}Te_{3.4}$ (ZT = 1.41 at 417 K)[9], liquid phase sintered $Ag_xBi_{0.5}Sb_{1.5}Te_3$ (1.36 at 400 K)[10], melt-spun $Bi_{0.5}Sb_{1.5}Te_3$ (1.24 at 350 K[11]) and n-type bismuth tellurides such as the CuI-doped $Bi_2Te_{2.7}Se_{0.3}$ (1.07 at 423 K)[12], Ag_8SnSe_6-incorporated $Bi_2Te_{2.69}Se_{0.33}Cl_{0.03}$ (1.24 at 353 K)[13], graphitic carbon nitride-decorated $Bi_2Te_{2.7}Se_{0.3}$ (1.29 at 400 K)[14], *etc.* However, thermoelectric energy conversion efficiency of bismuth tellurides remains insufficient for broader applications. Therefore, efficient and practical strategies to further improve ZT values are required[1,2,4].

During two decades, the phonon-glass and electron-crystal (PGEC) concept has been investigated as of critical importance in thermoelectric materials development[15]. The PGEC in Bismuth Tellurides has been adopted by incorporating nanoparticle distribution in the matrix. However, the nanoparticle distribution in the $Bi_{0.4}Sb_{1.6}Te_3$ (BST) matrix mainly focused on the decreasing κ_L rather than the increase of electrical transport property. Here we adopt the heavy metallic high entropy alloy composite to realize the PGEC in the BST matrix.

High-entropy alloys (HEAs), which consist of the multi-component mixing of five or more elements in near-equimolar concentrations, are considered promising candidates for high-performance thermoelectric materials. Their potential arises from low κ_L due to lattice distortions caused by atomic mass and size mismatches[16,17]. HEAs exhibit unique properties such as exceptional strength, ductility, and thermal stability, making them attractive for thermoelectric applications in extreme environmental conditions[18-20].

Recent advances in TE performance using the HEA concept have been introduced, including the n-type PbSe-based high-entropy material ($Pb_{0.89}Sb_{0.012}Sn_{0.1}Se_{0.5}Te_{0.25}S_{0.25}$, ZT = 1.8 at 900 K)[21], p-type PbSe-based high-entropy material ($Pb_{0.935}Na_{0.025}Cd_{0.04}Se_{0.5}S_{0.25}Te_{0.25}$, ZT = 2.0 at 900 K)[22], and p-type GeTe based high-entropy material ($Ge_{0.61}Ag_{0.11}Sb_{0.13}Pb_{0.12}Bi_{0.01}Te$, ZT = 2.7 at 750 K)[23] On the other hand, the HEA concept has not yet been successful in improving the TE performance of bismuth tellurides for room-temperature applications[17].

Here we investigated the anisotropic thermoelectric properties of the composites consisting of p-type bismuth antimony telluride (BST: Te-excess $Bi_{0.4}Sb_{1.6}Te_3$) and heavy metallic HEA nanoparticles (HEA: $TaNb_2HfZrTi$). Since the Te-excess effectively enhances the TE performance of the p-type bismuth antimony telluride[9,11], the composition of the $Bi_{0.4}Sb_{1.6}Te_3$ with additional Te was used for the BST matrix. The $TaNb_2HfZrTi$ is one of the representative HEAs with a body-centered cubic (BCC) phase and high mechanical strength[24]. To minimize a chemical doping effect, which can decrease the ZT value by deviating from the optimized carrier concentration, a mixed powder with the BST and HEA was used in the hot-press sintering process. The carrier concentrations, Seebeck coefficients (S), and Fermi energies (E_F) of the$BST+HEA_x$ (x = 0, 0.1, 0.5, 1.0 vol%) samples are not significantly affected by the addition of HEA. On the other hand, the significantly enhanced electrical conductivity σ and reduced κ_L are observed in the x = 0.1 vol% sample for the parallel (Pa) direction to the hot-press direction. The enhanced Pa-direction σ and the decrease of κ_L of the$BST+HEA_x$ samples are mainly affected by the enlarged carrier mean free paths λ_e and decrease of phonon mean free path λ_{ph}, which is a realization of PGEC[15]. The increased λ_e can be explained by the improved grain connectivity due to the HEA nanoparticles for the Pa-direction of the BST grains. Grain connectivity, which refers to the interconnection between grains, has a significant impact on transport characteristics[25-29]. The increased λ_{ph} in the$BST+HEA_x$ samples further supports that the HEA nanoparticles can improve the grain connectivity of the BST grains. As a result, the ZT values of the$BST+HEA_x$ samples are enhanced from 1.09 (x = 0) to 1.33 (x = 0.1 vol%) at 350 K in the Pa-direction due to the improved σ and reduced κ_L. These results clearly show that incorporating HEA nanoparticles is a promising strategy for improving the performance of the anisotropic thermoelectric materials. Additionally, controlling of the grain connectivity could be a good concept to improve the transport characteristics in various materials such as superconductors[30], batteries[31,32], solar cells[33,34], and semiconductors[35,36].

EXPERIMENTAL

Materials

The polycrystalline Te-excess BST samples were synthesized using the conventional melting method. The stoichiometric amounts of Bi (99.999%), Sb (99.999%), and Te (99.999%) were sealed in evacuated quartz tubes under high vacuum with the excess tellurium (~7 W%)[9]. The elements in the quartz ampule were melted at 923 K for 24 h and then water-quenched. The obtained ingots were pulverized into the powder using an agate mortar and pestle under an argon atmosphere. The $TaNb_2HfZrTi$ HEA powders were synthesized by the planetary ball milling method using powder elements. The stoichiometric ratios of Ta (99.98%), Nb (99.8%), Hf (99.6%), Zr (99.5%), and Ti (99.5%) powders were loaded into a stainless-steel jar with stainless-steel balls under an argon atmosphere. The ball milling process was carried out at a rotation speed of 400 rpm for 12 h[24].

The obtained BST and HEA (0, 0.1, 0.5 and 1.0 vol%) powders were mixed using a physical multimixer in vibration mode for 24 h. The mixed powders were loaded into a graphite die with an inner diameter of 15 mm and sintered using the hot-press method at 763 K under uniaxial pressure of 50 MPa for 60 min. The relative densities of the sintered samples were above 95% compared to the calculated densities.

Measurements

Since the BST exhibits anisotropic characteristics due to its layer structure, the thermoelectric properties and X-ray diffraction (XRD) patterns of the sintered samples were measured along the Pa and perpendicular (Pe) directions to the applied pressure direction of the hot press. The XRD patterns for the Pa- and Pe-directions were obtained using the Cu-$\kappa\alpha$ radiation (D8 advance, Bruker, Germany). High-resolution transmission electron microscopy (HR-TEM, JEM-ARM200F, JEOL, Japan) coupled with energy-dispersive X-ray (EDX) spectroscopy was used for the nanostructure analysis.

The temperature-dependent electrical resistivities (ρ = 1/σ) and S were simultaneously measured under a helium atmosphere using a thermoelectric properties measurement system (ZEM-3, ULVAC-RIKO, Japan). The Hall carrier concentrations (n_H) were obtained by the relations of n_H = -1/(R_He), where R_H (= ρ_{xy}/H) is the Hall coefficient, e is the elementary charge, ρ_{xy} is the Hall resistivity, and H is the applied magnetic field. The ρ_{xy} was measured by the fore-probe contact method under sweeping magnetic fields from -1 T to 1 T using a physical property measurement system (PPMS Dynacool 14 T, Quantum Design, USA). The κ_{total} was obtained using $\kappa = \rho_s \lambda C_p$, where ρ_s, λ, and C_p are sample density, thermal diffusivity, and specific heat, respectively. The λ was measured using a laser flash method (LFA-457, NETZSCH, Germany). The densities of the sintered samples were determined from their mass and dimensions. The C_p was measured using differential scanning calorimetry (DSC, NEXTA DSC200, HITACHI, Japan).

RESULTS AND DISCUSSION

Figure 1 shows the XRD patterns of the hot-pressedBST+HEA_x (x = 0, 0.1, 0.5, and 1.0 vol%) samples for the Pa and Pe -directions. The XRD peaks of the BST+HEA_x samples are normalized to the highest (015) peaks to compare the intensity of the (00*l*) peaks. The XRD patterns of the BST+HEA_x samples exhibit a rhombohedral structure with the lattice parameters (a ~4.296 Å, c ~30.496 Å), without any obvious impurities and significant changes in lattice parameters due to the HEA additions. The XRD peaks of the HEA powder show the BCC structure with the lattice parameter (a ~3.37 Å). The XRD patterns and the lattice parameters of the BST and HEA powder are consistent with previously reported results in the literature.[9,11,12,24,37] The intensities of the (00*l*) peaks for the Pa-direction are higher than those of the Pe-direction. This indicates that more BST layers are stacked along the Pa-direction due to the preferred orientation of the layer structure of the bismuth telluride[9,11,12,38,39]. The XRD peaks of the HEA in the composite samples (BST+HEA_x, x = 0.1, 0.5, and 1.0 vol%) are not detectable due to the small amount of HEA additions. The size of the HEA nanoparticles is estimated to be 4.6 nm, calculated using the Williamson-Hall relation based on the peak broadening of the XRD peaks[24].

Figure 2A and B shows the HR-TEM image of the HEA nanoparticles and the BST matrix in the x = 0.1 vol% sample, respectively. The HEA nanoparticles were identified using EDX measurements, as shown in the inset of Figure 2A. The lattice spacing (~0.33 nm) of Figure 2B corresponds to the (009) plane of the BST structure. The TEM image and the elemental mapping results in Figure 2C and Supplementary Figure 1 indicate that the nanometer-scale HEA nanoparticles are randomly and homogeneously distributed within the micrometer-scale BST matrix without agglomeration.

Figure 3A presents the temperature-dependent electrical conductivities [σ(T)] of the hot-pressed BST+HEA_x samples for the Pa- and Pe-directions. The obtained σ(T) values exhibit highly degenerate semiconducting behavior for the Pa- and Pe-directions. The σ of the pristine BST (550 S cm^{-1} for the Pa-direction, 770 S cm^{-1} for the Pe-direction at room temperature) are comparable with the literature values (500~700 S cm^{-1} for the Pa-direction, 650~850 S cm^{-1} for the Pe-direction at room temperature)[11]. The σ of the Pa-direction of the BST+HEA_x samples is significantly enhanced by the additions of the HEA

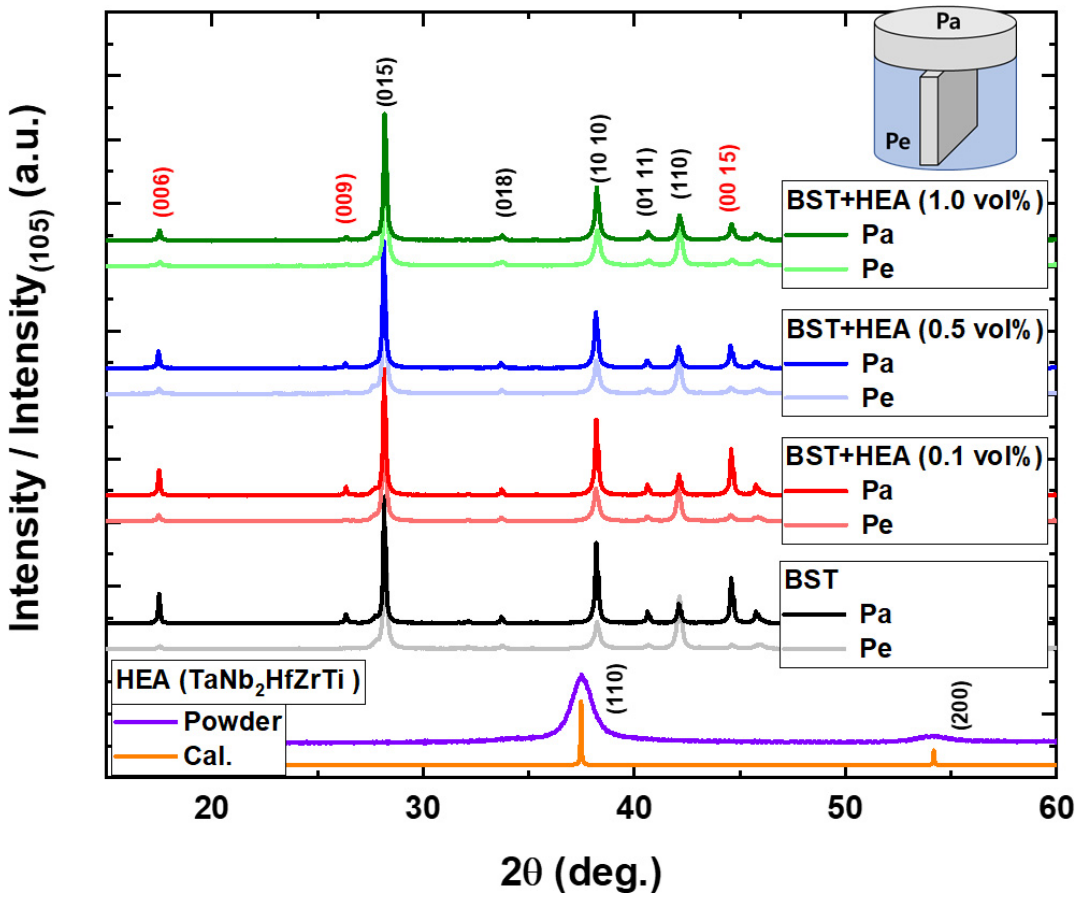

Figure 1. XRD patterns of the BST+HEA$_x$ (x = 0, 0.1, 0.5, and 1.0 vol%) for the Pa- and Pe-directions, the ball-milled $TaNb_2HfZrTi$ high entropy alloy (HEA) powder and the calculated data. XRD: X-ray diffraction.

nanoparticles. The enhancements of the σ are primarily attributed to the metallic characteristics of the $TaNb_2HfZrTi$ HEA (sintered HEA: σ ~12,500 S cm^{-1} at 300 K)[24]. Besides, the effect of σ for the HEA addition is not as pronounced in the Pe-direction of the BST+HEA$_x$ samples. Since there is no clear trend, the changes in the Pe-direction electrical conductivity of the BST+HEA composite can be attributed to experimental error.

The temperature-dependent Seebeck coefficients [S(T)] of the hot-pressed BST+HEA$_x$ (x = 0, 0.1, 0.5, and 1.0 vol%) samples for the Pa-direction and Pe-direction are presented in Figure 3B. The S(T) values show maxima due to the bipolar effect caused by the narrow bandgap (~0.1 eV) of the bismuth tellurides[40]. The S values of the pristine BST (224 for the Pa-direction, 216 μV K^{-1} for the Pe-direction at room temperature) are comparable with the literature values (235~245 μV K^{-1} for the Pa-direction, 215~230 μV K^{-1} for the Pe-direction at room temperature)[11]. The S of the sintered HEA ($TaNb_2HfZrTi$) sample is S = 5.7 μV K^{-1} at 300 K. The S values of the BST+HEA$_x$ samples are not significantly affected by the additions of the HEA nanoparticles.

The temperature-dependent power factors [$S^2\sigma$(T)] of the BST+HEA$_x$ samples for the Pa- and Pe-directions are presented in Figure 3C. The $S^2\sigma$(T) values of the Pe-direction are higher than those of the Pa-direction due to the higher electrical conductivity resulting from the preferred orientations of the BST layers. The $S^2\sigma$ of the pristine BST (2.7 mW m^{-1} K^{-2} for the Pa-direction, 3.6 mW m^{-1} K^{-2} for the Pe-direction at room

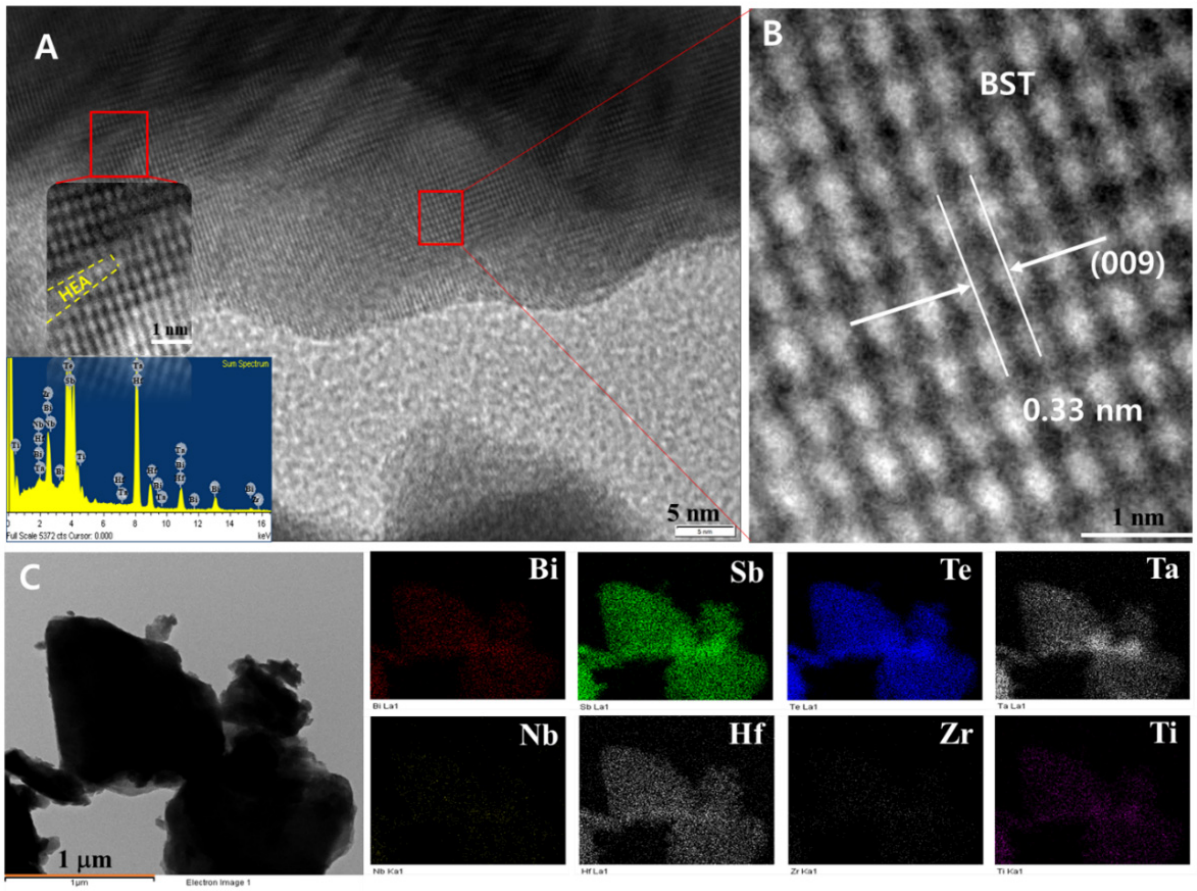

Figure 2. (A) High-resolution transmission electron microscopy (HR-TEM) image of the HEA nanoparticles and BST matrix in the BST+HEA$_x$ (x = 0.1 vol%) sample; (B) the lattice sparing corresponding to the (009) plane of the BST structure; (C) the TEM image of the x = 0.1 vol% sample with the elemental mapping of bismuth (Bi), antimony (Sb), tellurium (Te), tantalum (Ta), niobium (Nb), hafnium (Hf), zirconium (Zr), and titanium (Ti). HEA: High entropy alloy; BST: $Bi_{0.4}Sb_{1.6}Te_3$.

temperature) are comparable to the literature values (3.0~3.6 mW m^{-1} K^{-2} for the Pa-direction, 3.5~4.2 mW m^{-1} K^{-2} for the Pe-direction at room temperature)[11]. The $S^2\sigma$ values are clearly enhanced at the lower HEA concentration (x = 0.1 vol%), but the effects of the HEA additions are not clearly evident at the higher concentrations.

The enhanced $S^2\sigma$ by the additions of the HEA nanoparticles are primarily attributed to the increased σ, as shown in Figure 3D. The S of the BST+HEA$_x$ samples do not show significant changes (within a 5% error) by the additions of the HEA below 1.0 vol%. However, the σ values of the BST+HEA$_x$ samples are significantly affected by the HEA additions. Notably, the highest σ is observed in the low HEA concentration sample (x = 0.1 vol%), and the σ values for the Pa-direction are significantly enhanced compared to those for the Pe-direction with the HEA additions. The enhanced σ for the Pa-direction clearly indicates that the metallic HEA nanoparticles effectively increase the electrical conductivity in the out-of-plane direction of the BST.

The different parts of the BST+HEAx (x = 0.1 vol%) were measured for the Pa-direction as shown in Supplementary Figure 2. The comparable σ(T), S(T) and $S^2\sigma$(T) of the Pa-1 and Pa-2 of the BST+HEAx (x = 0.1 vol%) sample indicate that the HEA nanoparticle is homogeneously separated in the sample.

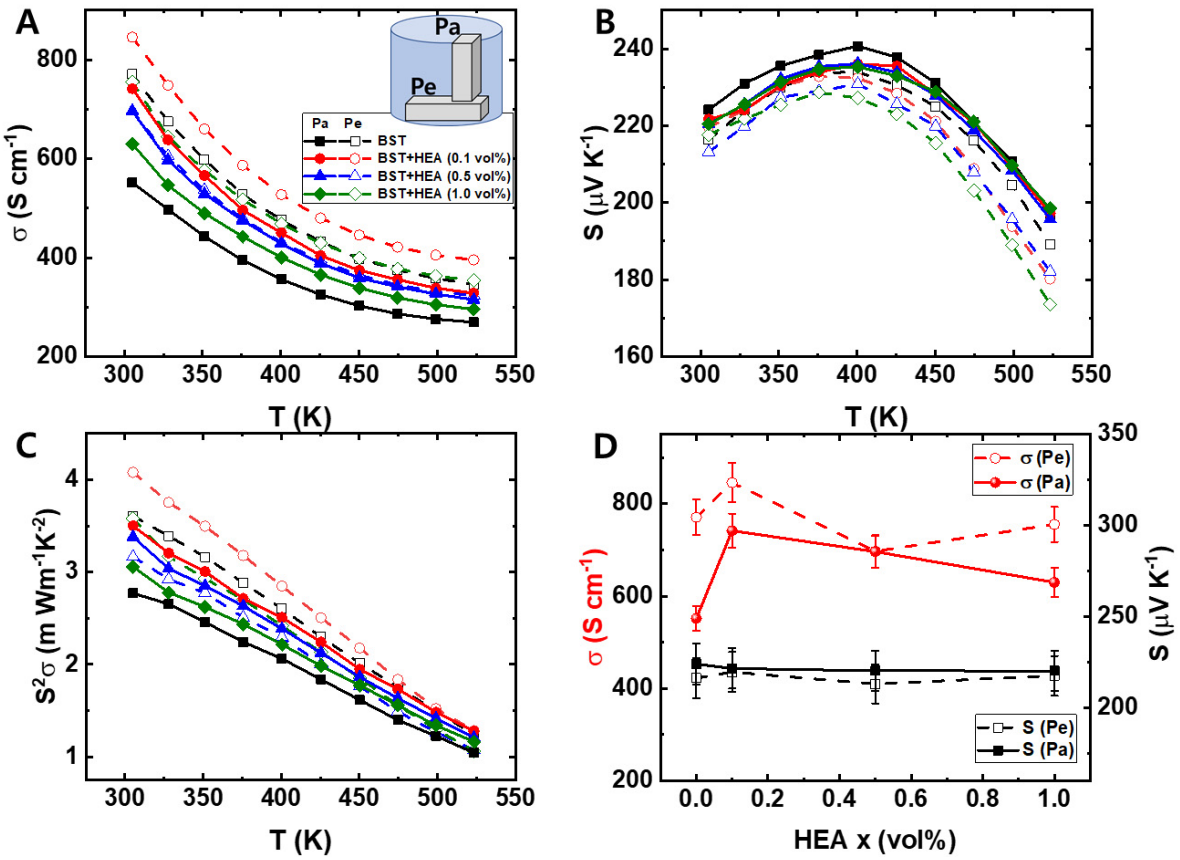

Figure 3. (A) Temperature-dependent electrical conductivities σ(T); (B) Seebeck coefficients S(T); (C) temperature-dependent power factors $S^2\sigma(T)$ of the BST+HEA_x (x = 0, 0.1, 0.5, and 1.0 vol%) samples for the Pa- and Pe-directions; (D) room-temperature electrical conductivities and Seebeck coefficients as a function of the HEA concentrations (error bar: 5%). BST: $Bi_{0.4}Sb_{1.6}Te_3$.; HEA: high entropy alloy.

Figure 4A shows that the n_H of the hot-pressed BST+HEA_x (x = 0, 0.1, 0.5, and 1.0 vol%) samples are slightly enhanced at the 0.1 vol% sample, but are not significantly affected in the range from 0.5 vol% to 1.0 vol%. The trends in the n_H values of the BST with the HEA additions are notably different compared to those with other doping elements such as Ni, Sn[41], Pb, Fe, Co[37] and Ag[10], as shown in Figure 4B. The less susceptible n_H values of the BST+HEA_x samples suggest that the HEA nanoparticles exist in the BST matrix without significant chemical reactions that would alter the carrier concentrations. This behavior is attributed to the structural stability of the HEA nanoparticles[20]. The stable structural phase of the HEA nanoparticles may promote the formation of an ideal composite with BST, without inducing chemical doping effects. Further detailed investigations are required to understand the unchanged carrier concentrations in the BST+HEA composite.

Using $\sigma = ne\mu$, where n, e, and μ are the carrier concentration, elementary charge, and carrier mobility, respectively[2,5], the Hall mobilities (μ_H) of the BST+HEA_x samples were investigated. Figure 4C shows that the enhancements in the μ_H are observed in the Pa-direction at low HEA concentrations, in contrast to the less susceptible μ_H of the Pe-direction. Although the μ_H is enhanced to the Pa-direction, the μ_H values of the BST with the HEA additions are not significantly changed compared to those with other doping elements such as Ni, Sn[41], Pb, Fe, Co[37] and Ag[10], as shown Figure 4D.

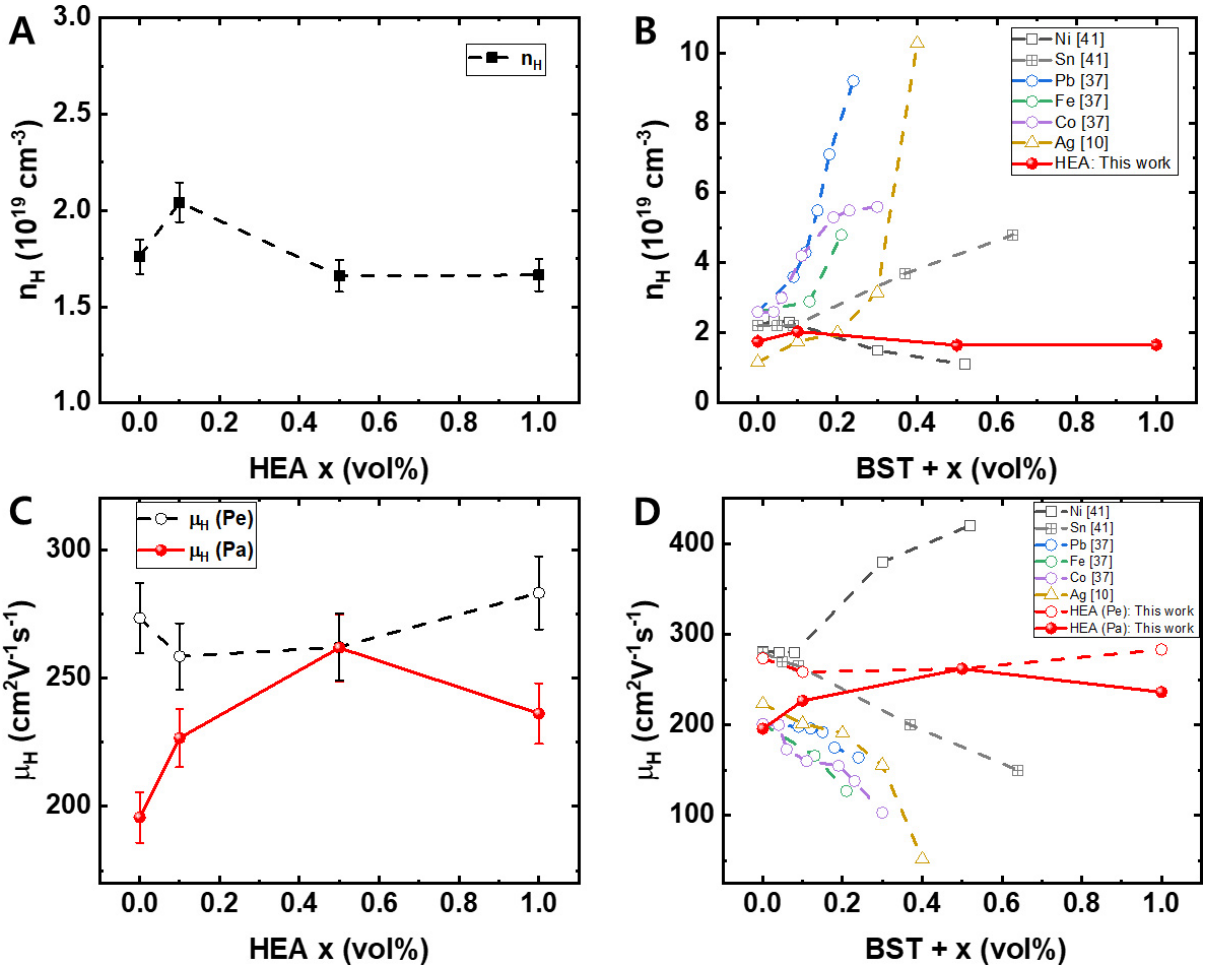

Figure 4. (A) Room-temperature Hall carrier concentrations n_H as a function of the HEA concentrations; (B) carrier concentrations n_H for the various doping elements: Ni, Sn[41], Pb, Fe, Co[37], Ag[10]; (C) room-temperature Hall mobilities μ_H as a function of the HEA concentrations; (D) mobilities μ_H for the various doping elements: Ni, Sn[41], Pb, Fe, Co[37], Ag[10]. HEA: High entropy alloy.

Figure 5A presents the effective masses of carrier m^* of the hot-pressed BST+HEA$_x$ samples, obtained by the Pisarenko relation[2,5]. Although the S change of the BST+HEA$_x$ is insignificant, the m^* is slightly enhanced at the lower HEA concentration (x = 0.1 vol%). Still, it has slightly decreased at the higher HEA concentrations (x = 0.5 and 1.0 vol%). The enhanced m^* at the lower HEA concentration (x = 0.1 vol%) can be attributed to the resonant state effect[2,5]. However, further detailed investigations are needed to clarify these effects.

Using the S, Hall carrier mobilities μ_H, and effective masses of carrier m^*, the mean free paths of carrier λ_e, and the E_F of the hot-pressed BST+HEA$_x$ (x = 0, 0.1, 0.5, and 1.0 vol%) samples were calculated [Figure 5B] using

$$\lambda_{mfp} = \left(\frac{\mu}{e}\right)\sqrt{2E_F m^*} \quad (1)$$

$$E_F = \left(r + \frac{3}{2}\right)\frac{\pi^2 k_B^2 T}{3eS} \quad (2)$$

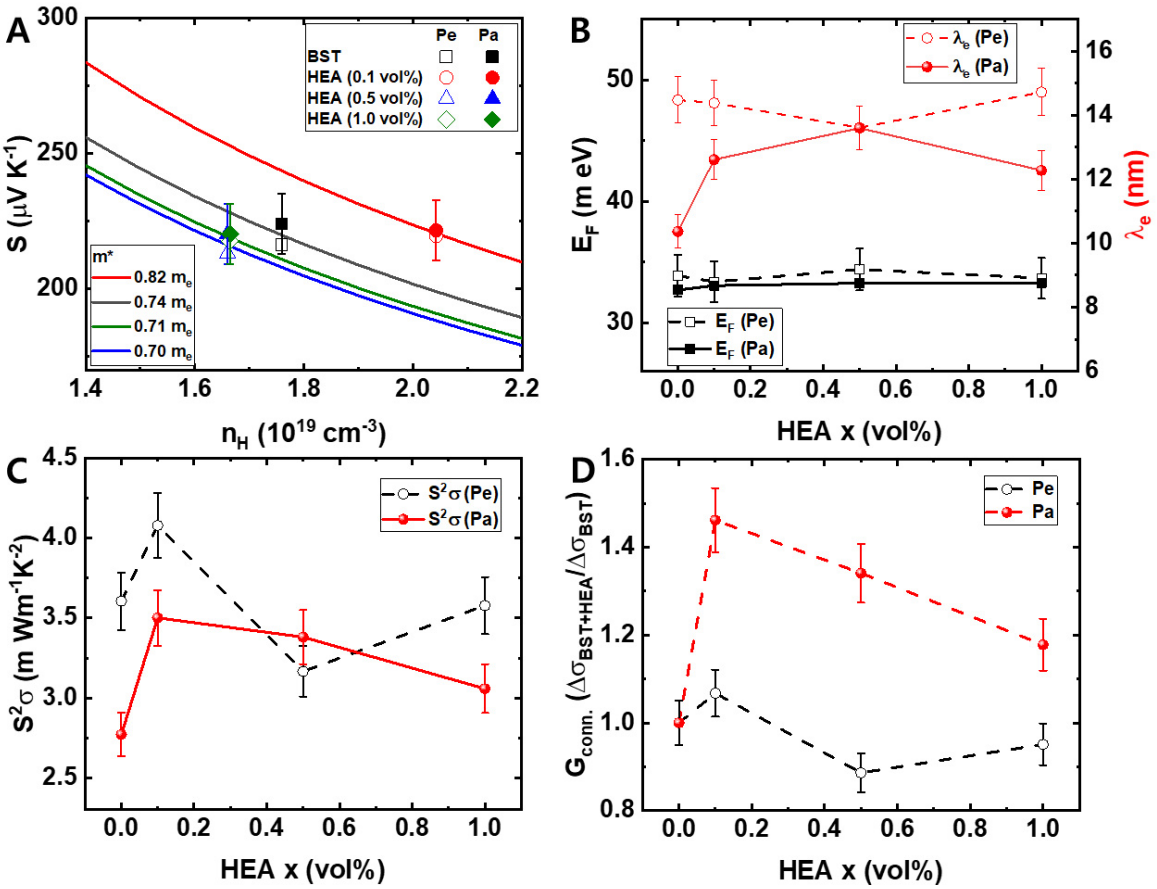

Figure 5. (A) Seebeck coefficients as a function of n_H with the Pisarenko plots of the hot-pressed BST+HEA$_x$ (x = 0, 0.1, 0.5, and 1.0 vol%) samples for the Pa- and Pe-directions; (B) Fermi energies E_F and the mean free paths of the carrier λ_e; (C) room-temperature power factors $S^2\sigma$; (D) electrical grain connectivity $G_{conn.}$ as a function of the HEA concentrations at room temperature. HEA: High entropy alloy; BST: $Bi_{0.4}Sb_{1.6}Te_3$.

where r is the scattering factor (r = -1/2 for acoustic phonon scattering)[39,42]. The E_F is not significantly affected by the additions of the HEA nanoparticles in the BST matrix, as presented in Table 1. In contrast to the less susceptible λ_e for the Pe-direction, the λ_e in the Pa-direction of the BST+HEA is increased compared to the pristine BST. The results of the λ_e clearly show that the HEA nanoparticle distribution is effective for enhancing the σ in the Pa-direction of the BST through the increased λ_e.

The enhanced λ_e, without the changes in the n_H and E_F, can be attributed to the effect of the enhanced electrical grain connectivity[25,27,28]. Since the BST grains and the HEA nanoparticles are homogeneously mixed in the BST+HEA samples, the electrical resistivities of the BST+HEA are strongly affected by the metallic HEA nanoparticles.

The temperature-dependent scattering of the electrical resistivity can be roughly estimated by the characteristic change in the resistivity $\Delta\rho = \rho(T_{high}) - \rho(T_{low})$[25,27,28]. Using the temperature-dependent electrical resistivities $\rho(T)$ of the BST+HEA$_x$ samples, the characteristic change in the resistivities $\Delta\rho$ was obtained, as shown in Supplementary Figure 3A and B. However, the $\Delta\rho$ does not provide a clear understanding of the electrical transport characteristics of the composites. To address this, a modified factor for the electrical grain connectivity $G_{conn.}$ is introduced to quantify the contribution of the grain connectivity

Table 1. Mean free paths of the carrier λ_e, Fermi energies E_F, the phonon mean free path λ_{Ph}, and average phonon scattering time τ_{ph} of the BST+HEA$_x$ samples

Sample	E_f (eV)	λ_e (nm)	λ_{Ph} (nm)	τ_{ph} (s 10^{-12})
Pa - 0	32.7	10.4	5.3	2.88
Pa - 0.1	33.1	12.6	4.9	2.88
Pa - 0.5	33.3	13.6	5.6	2.94
Pa - 1.0	33.3	12.3	6.1	2.95
Pe - 0	33.9	14.5	6.1	2.49
Pe - 0.1	33.4	14.4	5.8	2.16
Pe - 0.5	34.4	13.6	6.3	2.51
Pe - 1.0	33.7	14.7	6.6	3.08

HEA: High entropy alloy; BST: $Bi_{0.4}Sb_{1.6}Te_3$.

to the electrical conductivity,

$$G_{conn.} = \frac{\Delta\sigma_{BST+HEA}}{\Delta\sigma_{BST}} \quad (3)$$

where $\Delta\sigma = \sigma(T_{low}) - \sigma(T_{high})$ is the characteristic change in the electrical conductivity for the BST+HEA samples. In this work, the T_{low} = 300 K and T_{high} = 500 K are used for the σ(T) of the pristine BST and BST+HEA samples.

The tendencies of the $S^2\sigma$ of the BST+HEA$_x$ samples with the HEA additions for the Pa- and Pe-directions are shown in Figure 5C. The trends in the $S^2\sigma$ align well with the $G_{conn.}$ as a function of the HEA concentrations for the Pa- and Pe-directions, as shown in Figure 5D. The Pa-direction $G_{conn.}$ is enhanced by the HEA nanoparticle, whereas the Pe-direction $G_{conn.}$ is not significantly affected. These trends are consistent with the results for the λ_e. The enhanced G_{conn} and λ_e clearly indicate that the HEA nanoparticles are more effective in increasing the electrical grain connectivity of BST in the Pa-direction, which originally exhibits lower electrical conductivity compared to the Pe-direction. Therefore, the power factor can be enhanced through increased electrical conductivity without a change in carrier concentration due to the improved $G_{conn.}$ induced by the addition of HEA nanoparticles in the BST matrix.

The temperature-dependent κ_{total} [κ_{total}(T)] of the hot-pressed BST+HEA$_x$ (x = 0, 0.1, 0.5, and 1.0 vol%) samples for the Pa- and Pe-directions is shown in Figure 6A. The thermal conductivity of the sintered HEA ($TaNb_2HfZrTi$) sample is κ = 10.25 W $m^{-1}K^{-1}$ at 300 K. The κ_{total}(T) of the BST+HEA$_x$ samples decreases with increasing temperature near room temperature. The κ_{total}(T) is increased with an increasing temperature above 350 K due to the bipolar effect, consistent with the previous reports[9,11]. The lower Pa-direction κ_{total}(T) compared to the Pe-direction κ_{total}(T) is attributed to the anisotropic alignment of the BST layers at low HEA concentration (below 0.5 vol%). Also, the κ_{total}(T) values for the Pa- and Pe-directions are similar at the higher HEA concentration (1.0 vol%).

The κ_{total} of the bismuth telluride is primarily affected by the phonons κ_L, electrons κ_e, and bipolar diffusion κ_b. Using the Wiedemann-Franz law (κ_e = LσT, where L, σ, T are the Lorenz number, electrical conductivity and absolute temperature, respectively.), the electronic thermal conductivity κ_e can be calculated. The Lorenz number $L_0 = (\pi^2/3)(k_B/e)^2 = 2.45 \times 10^{-8}$ W Ω K^2 can be assumed for a simple metal; however, it should be modified in case of correlated metals or degenerated semiconductors. Figure 6B presents the calculated Lorenz numbers L(T) for correlated metals and degenerated semiconductors, as calculated using[38,39]

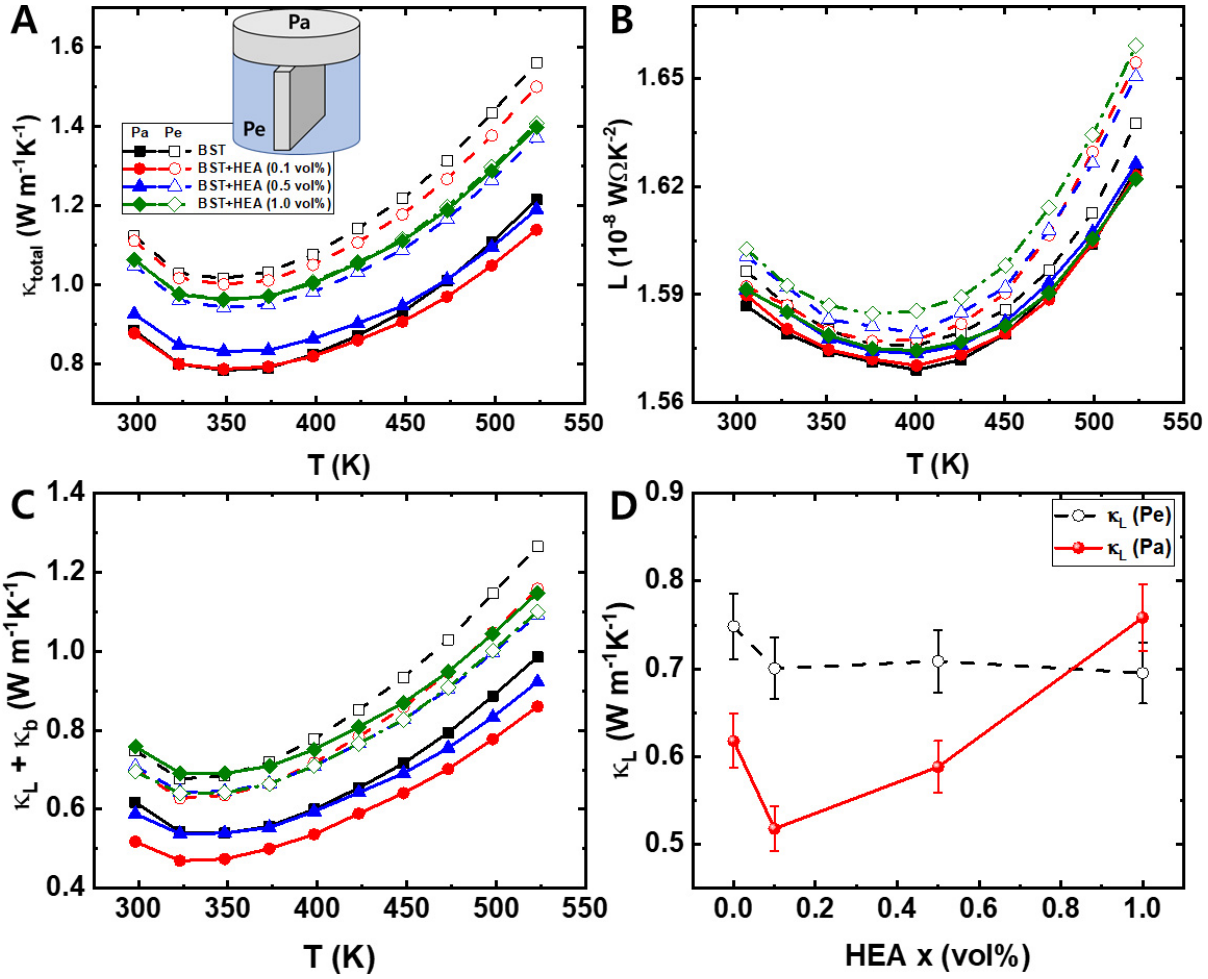

Figure 6. (A) Temperature-dependent total thermal conductivities κ_{total}(T); (B) temperature-dependent Lorenz numbers L(T); (C) temperature-dependent lattice and bipolar thermal conductivities $\kappa_L + \kappa_b$(T) of the hot-pressed BST+HEA$_x$ (x = 0, 0.1, 0.5, and 1.0 vol%) samples for Pa- and Pe-directions; (D) room-temperature lattice thermal conductivities κ_L as a function of the HEA concentrations. HEA: High entropy alloy; BST: $Bi_{0.4}Sb_{1.6}Te_3$.

$$S = \frac{k_B}{e}\left(\frac{\left(r + \frac{5}{2}\right)F_{r+\frac{3}{2}}(\eta)}{\left(r + \frac{3}{2}\right)F_{r+\frac{1}{2}}(\eta)} - \eta\right) \tag{4}$$

$$F_n(\eta) = \int_0^\infty \frac{\chi^n}{1 + e^{\chi-\eta}} d\chi \tag{5}$$

$$L = \left(\frac{k_B}{e}\right)^2 \left\{\frac{\left(r + \frac{7}{2}\right)F_{r+\frac{5}{2}}(\eta)}{\left(r + \frac{3}{2}\right)F_{r+\frac{1}{2}}(\eta)} - \left[\frac{\left(r + \frac{5}{2}\right)F_{r+\frac{3}{2}}(\eta)}{\left(r + \frac{3}{2}\right)F_{r+\frac{1}{2}}(\eta)}\right]^2\right\} \tag{6}$$

where S is the temperature-dependent Seebeck coefficient, $F_n(\eta)$ is the n-th order Fermi integral, r is scattering parameter (r = -1/2 for the acoustic phonon scattering), and $\eta = E_F/k_BT$ is the reduced E_F[38,39].

By subtracting the κ_e from κ_{total}, the temperature-dependent lattice and bipolar thermal conductivities $\kappa_L+\kappa_b(T)$ of the hot-pressed BST+HEA$_x$ samples for the Pa- and Pe-directions are obtained, as shown Figure 6C. The $\kappa_L+\kappa_b(T)$ shows the conventional 1/T behavior near room temperature and the bipolar effect above 350 K. The 1/T behavior of the thermal conductivity is primarily caused by the Umklapp processes of acoustic phonon[39]. The thermal conductivity of narrow bandgap materials increases with temperature due to the bipolar effect, which is associated with thermally excited minority carriers at high temperatures. The bipolar effect is associated with the narrow bandgap (~0.1 eV) of bismuth tellurides at high temperatures[40]. Therefore, the κ_L dominates near room temperature in the $\kappa_L+\kappa_b(T)$ of the BST+HEA$_x$ samples.

Figure 6D shows the lattice thermal conductivities κ_L of the BST+HEA$_x$ samples for the Pa- and Pe-directions at 300 K. While the Pe-direction κ_L are slightly reduced, the κ_L of the Pa-direction are clearly decreased by the HEA nanoparticles below 0.5 vol% but noticeably increase at 1.0 vol%. The increased Pa-direction κ_L in the BST+HEA composites is attributed to enhanced grain connectivity, consistent with the results for λ_e. Interestingly, the Pa-direction κ_L of pure BST is lower than that of the Pe-direction due to the preferred orientation of the BST layers. However, in the BST+HEA composite with 1.0 vol% HEA, the Pa-direction κ_L becomes higher than the Pe-direction κ_L. This unconventional increase in Pa-direction κ_L supports the idea that HEA nanoparticles enhance grain connectivity along the Pa-direction in the BST matrix.

The lattice thermal conductivities κ_L can be described by the Debye-Callaway model using

$$\kappa_L = \frac{k_B}{2\pi^2 v}\left(\frac{k_B T}{\hbar}\right)^3 \int_0^{\Theta/T} \frac{x^4 e^x}{\tau_C^{-1}(e^x-1)^2}\,dx \tag{7}$$

where Θ is the Debye temperature, τ_C is the total scattering time rate, and v is the sound velocity. The scattering time τ_C, which is associated with boundary scattering, point defect scattering, and Umklapp scattering, can be expressed as follows

$$\tau_C^{-1} = \frac{v}{L} + \frac{V\omega^4}{4\pi v^3}\Gamma + A_N \frac{2}{(6\pi^2)^{1/3}}\frac{V^{1/3}\gamma^2\omega^2 T}{M v^3} \tag{8}$$

where L is the average diameter of grain boundary, ω is phonon frequency, V is the lattice volume, Γ is the scattering parameter of a point defect, A_N is the free parameter of Umklapp scattering, γ is the Grüneisen parameter, and M is the average atomic mass.[43]

The thermal conductivity due to the bipolar contribution can be expressed as follows

$$\kappa_b = B\exp\left(-\frac{E_g}{2k_B T}\right) \tag{9}$$

where B is a fitting parameter[44].

Based on the theoretical equations for the κ_L and κ_b along with the parameters (in Supplementary Table 1) such as the average group velocity of a phonon (v = 2147 /s), acoustic Debye temperature (Θ = 94 K), and Grüneisen parameter (γ = 2.3)[43], the lattice and bipolar thermal conductivities $\kappa_L+\kappa_b(T)$ were calculated using the fitting method. The fitting results are presented in Supplementary Figure 4A and B for the Pa- and Pe-directions, respectively. The calculated κ_L and κ_b are shown separately in Supplementary Figure 4C and D. The obtained parameters are listed in Supplementary Table 1.

From the Debye-Callaway model and the obtained fitting parameters, the λ_{Ph} and average phonon scattering time τ_{ph} can be obtained using

$$\lambda_{Ph} = v\tau_{ph}^{avg} \tag{10}$$

$$\tau_{Ph} = \frac{\int_0^{\frac{\Theta}{T}} \frac{x^4 e^x}{\tau_C^{-1}(e^x-1)^2} dx}{\int_0^{\frac{\Theta}{T}} \frac{x^4 e^x}{(e^x-1)^2} dx} \tag{11}$$

The obtained λ_{Ph} and τ_{ph} are listed in Table 1. The λ_{Ph} follows the behavior of κ_L with HEA concentrations as presented in Table 1 and Figure 6D. The λ_{Ph} values decreased for x = 0.1 and monotonically increased with increasing the HEA concentration for both the Pa- and Pe-directions of the BST+HEA_x samples. The decreasing λ_{Ph} for x = 0.1 is due to the phonons' scattering between the BST matrix and nanoprecipitation of HEA. The increasing λ_{Ph} is consistent with the grain connectivity increase between the HEA nanoparticles and BST matrix.

Temperature-dependent ZT values of the hot-pressed BST+HEA_x (x = 0, 0.1, 0.5, and 1.0 vol%) samples for the Pa- and Pe-directions are presented in Figure 7A. The ZT values are increased with increasing temperature near room temperature but decrease above 350 K due to the bipolar effect. The ZT values of the BST+HEA_x samples are enhanced with the additions of the HEA nanoparticles below 0.5 vol%. The ZT value of the sintered HEA ($TaNb_2HfZrTi$) sample is ZT = 0.0012 at 300 K. Figure 7B clearly shows that the HEA additions in the BST matrix improve the TE performances below 0.5 vol%. In particular, the HEA nanoparticles are more effective at enhancing the ZT values of the BST in the Pa-direction. The ZT values in the BST with the HEA additions are increased from 0.93 (x = 0) to 1.23 (x = 0.1 vol%) for the Pa-direction at 300 K. Furthermore, the maximum ZT value (1.33 at 350 K) is observed in the 0.1 vol% sample for the Pa-direction.

The HEA nanoparticles effectively increase the electronic MFP λ_e in the Pa-direction, and decrease the λ_{Ph} in both Pe- and Pa-directions for $x \leq 0.5$, indicating the effective phonon glass and electron crystal by enhancing the grain connectivity and nanoparticle distribution in the BST matrix. The enhanced ZT value of the Pa-direction in the 0.1 vol% sample is caused by the increased electrical conductivity and decreased κ_L. The increase of the electrical conductivity is due to the enhanced λ_e and the reduced κ_L is due to the scattering of phonons (decrease of λ_{Ph}) for the HEA nanoparticle distributions.

Figure 7C and D shows the average ZT ($ZT_{avg.}$), which can be obtained by[3]

$$ZT_{avg.} = \frac{\int_{T_{cold}}^{T_{hot}} ZT dt}{T_{hot} - T_{cold}} \tag{12}$$

where T_{hot} and T_{cold} are the temperatures on the hot side and cold side, respectively. The $ZT_{avg.}$ is an important factor for real applications when the thermoelectric materials are exposed to thermal gradients. The maximum $ZT_{avg.}$ of the BST+HEA_x samples is 1.26 (0.1 vol%, Pa-direction) at the T_{hot} = 425K and T_{cold} = 300 K. The $ZT_{avg.}$ of the BST+HEA_x samples show higher TE performance compared to other reported values in the literature[37,41,45-51]. The high $ZT_{avg.}$ values achieved with the HEA additions in the BST indicate strong potential for practical applications under temperature gradients.

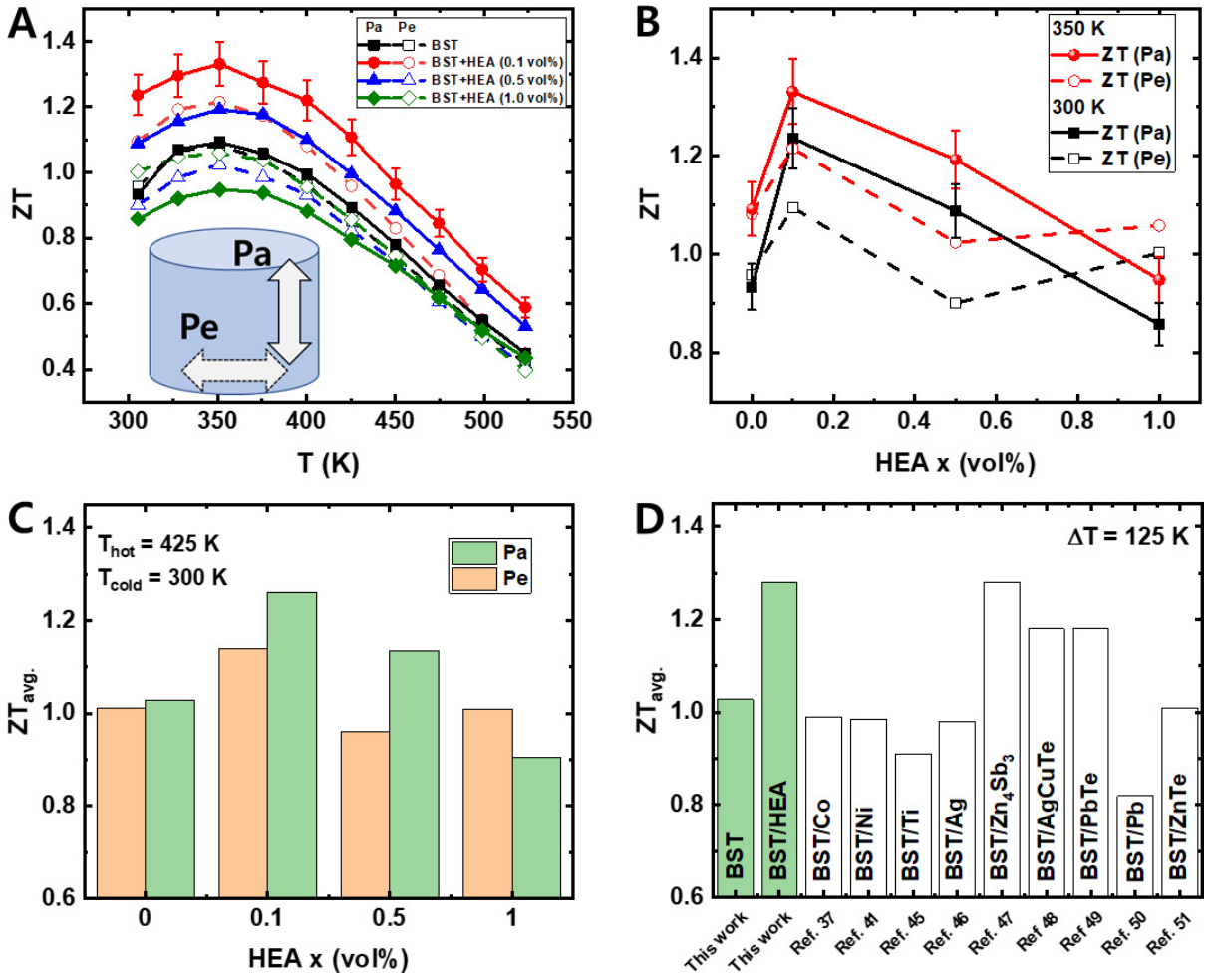

Figure 7. (A) Temperature-dependent figure of merit ZT of the hot-pressed BST+HEA_x (x = 0, 0.1, 0.5, and 1.0 vol%) samples for the Pa- and Pe-direction; (B) ZT values as a function of the HEA concentrations at 300 and 350 K; (C) maximum $ZT_{avg.}$ of the BST+HEA_x samples at the T_{hot} = 425K and T_{cold} = 300 K; (D) average ZT with the literature values[37,41,45-51]. BST: $Bi_{0.4}Sb_{1.6}Te_3$; HEA: high entropy alloy.

CONCLUSIONS

In summary, the anisotropic thermoelectric properties of the sintered BST+HEA_x (x = 0, 0.1, 0.5, and 1.0 vol%) samples were investigated. The homogeneously dispersed HEA nanoparticles in the BST matrix effectively increase the Pa-direction electrical conductivity, without reducing S. The small amounts of the HEA nanoparticles (below 0.5 vol%) efficiently enhance the mean free path of the carrier for the Pa-direction of the BST, without significantly altering the carrier concentration. The enhanced electrical conductivity due to the HEA additions can be attributed to the improved electrical grain connectivity in the Pa-direction of the BST. The HEA nanoparticles may reduce the electrical potential barriers of the Pa-direction at grain boundaries. The decrease of κ_L by scattering of phonons (decrease of λ_{ph}) with enhanced electronic mean free path λ_e for x = 0.1 sample shows the PGEC effect. As a result of the enhanced electrical conductivity and reduced κ_L with the HEA nanoparticle distribution, a maximum ZT = 1.33 at 350 K and high $ZT_{avg.}$ = 1.26 (T_{hot} = 425K and T_{cold} = 300 K) were obtained in the 0.1 vol% sample for the Pa-direction. The controlling grain connectivity through composites with HEA nanoparticles offers a promising strategy not only for achieving high ZT values but also for enabling industrial applications

DECLARATIONS

Authors' contributions

Investigation, data curation, formal analysis, methodology, writing - original draft: Kumar, A.
Investigation, data curation, formal analysis, writing - original draft: Thoravat, S.
Conceptualization, characterization, visualization, writing - review and editing: Yun, J. H.
Investigation, formal analysis: Park, J.; Jin, H.
Investigation, data curation, formal analysis: Hidayati, R.
Conceptualization, characterization, visualization, methodology, formal analysis, writing - original draft, writing - review and editing: Kim, J. H.
Conceptualization, funding acquisition, resources, supervision, writing - review and editing: Rhyee, J. S.
All authors analyzed the data and contributed to the discussions.

Availability of data and materials

Some results of supporting the study are presented in the Supplementary Materials. Other raw data that support the findings of this study are available from the corresponding author upon reasonable request.

Financial support and sponsorship

This research was supported by the National Research Foundation of Korea (NRF), funded by the Ministry of Education, Science and Technology (RS-2023-00247622 and NRF-2022M3C1A3091988).

Conflicts of interest

All authors declared that there are no conflicts of interest.

Ethical approval and consent to participate

Not applicable.

Consent for publication

Not applicable.

REFERENCES

1. Yan, Q.; Kanatzidis, M. G. High-performance thermoelectrics and challenges for practical devices. *Nat. Mater.* **2022**, *21*, 503-13. DOI PubMed
2. Shi, X. L.; Zou, J.; Chen, Z. G. Advanced thermoelectric design: from materials and structures to devices. *Chem. Rev.* **2020**, *120*, 7399-515. DOI PubMed
3. Hameed, M. M.; Mansor, M.; Azrin, M. A. M.; Muhsin, S. Thermoelectric cooler performance enhancement using thermoelectric generators and their use as a single model to improve the performance of thermal battery management systems for electric vehicles. *Energy. Storage.* **2023**, *5*, e406. DOI
4. Mao, J.; Chen, G.; Ren, Z. Thermoelectric cooling materials. *Nat. Mater.* **2021**, *20*, 454-61. DOI
5. Wu, Z.; Zhang, S.; Liu, Z.; Mu, E.; Hu, Z. Thermoelectric converter: strategies from materials to device application. *Nano. Energy.* **2022**, *91*, 106692. DOI
6. Hao, F.; Qiu, P.; Tang, Y.; et al. High efficiency Bi_2Te_3-based materials and devices for thermoelectric power generation between 100 and 300 °C. *Energy. Environ. Sci.* **2016**, *9*, 3120-7. DOI
7. Witting, I. T.; Chasapis, T. C.; Ricci, F.; et al. The thermoelectric properties of bismuth telluride. *Adv. Electron. Mater.* **2019**, *5*, 1800904. DOI
8. Hu, L.; Zhu, T.; Liu, X.; Zhao, X. Point defect engineering of high-performance bismuth-telluride-based thermoelectric materials. *Adv. Funct. Mater.* **2014**, *24*, 5211-8. DOI
9. Kim, Y. M.; Lydia, R.; Kim, J.; Lin, C.; Ahn, K.; Rhyee, J. Enhancement of thermoelectric properties in liquid-phase sintered Te-excess bismuth antimony tellurides prepared by hot-press sintering. *Acta. Mater.* **2017**, *135*, 297-303. DOI
10. Zhu, B.; Xie, W.; Huang, R.; et al. High thermoelectric performance in Ag-doped $Bi_{0.5}Sb_{1.5}Te_3$ nanocomposites synthesized via low-

temperature liquid phase sintering. *Mater. Today. Energy.* **2024**, *46*, 101717. DOI

11. Deng, R.; Su, X.; Zheng, Z.; et al. Thermal conductivity in $Bi_{0.5}Sb_{1.5}Te_{3+x}$ and the role of dense dislocation arrays at grain boundaries. *Sci. Adv.* **2018**, *4*, eaar5606. DOI
12. Cho, H.; Kim, J. H.; Back, S. Y.; Ahn, K.; Rhyee, J.; Park, S. Enhancement of thermoelectric properties in CuI-doped $Bi_2Te_{2.7}Se_{0.3}$ by hot-deformation. *J. Alloys. Compd.* **2018**, *731*, 531-6. DOI
13. Haruna, A. Y.; Luo, Y.; Li, W.; et al. High thermoelectric performance in multiscale Ag_8SnSe_6 included n-type bismuth telluride for cooling application. *Mater. Today. Energy.* **2023**, *35*, 101332. DOI
14. Luo, K.; Chen, H.; Hu, W.; et al. Tailoring interfacial states for improved n-type bismuth telluride thermoelectrics. *Nano. Energy.* **2024**, *128*, 109845. DOI
15. Beekman, M.; Morelli, D. T.; Nolas, G. S. Better thermoelectrics through glass-like crystals. *Nat. Mater.* **2015**, *14*, 1182-5. DOI PubMed
16. Wang, X.; Guo, W.; Fu, Y. High-entropy alloys: emerging materials for advanced functional applications. *J. Mater. Chem. A.* **2021**, *9*, 663-701. DOI
17. Ghosh, S.; Raman, L.; Sridar, S.; Li, W. High-entropy engineering in thermoelectric materials: a review. *Crystals* **2024**, *14*, 432. DOI
18. Ye, Y.; Wang, Q.; Lu, J.; Liu, C.; Yang, Y. High-entropy alloy: challenges and prospects. *Mater. Today.* **2016**, *19*, 349-62. DOI
19. George, E. P.; Raabe, D.; Ritchie, R. O. High-entropy alloys. *Nat. Rev. Mater.* **2019**, *4*, 515-34. DOI
20. Yao, Y.; Dong, Q.; Brozena, A.; et al. High-entropy nanoparticles: synthesis-structure-property relationships and data-driven discovery. *Science* **2022**, *376*, eabn3103. DOI
21. Jiang, B.; Yu, Y.; Cui, J.; et al. High-entropy-stabilized chalcogenides with high thermoelectric performance. *Science* **2021**, *371*, 830-4. DOI
22. Jiang, B.; Yu, Y.; Chen, H.; et al. Entropy engineering promotes thermoelectric performance in p-type chalcogenides. *Nat. Commun.* **2021**, *12*, 3234. DOI PubMed PMC
23. Jiang, B.; Wang, W.; Liu, S.; et al. High figure-of-merit and power generation in high-entropy GeTe-based thermoelectrics. *Science* **2022**, *377*, 208-13. DOI
24. Kim, J. H.; Hidayati, R.; Jung, S.; et al. Enhancement of critical current density and strong vortex pinning in high entropy alloy superconductor $Ta_{1/6}Nb_{2/6}Hf_{1/6}Zr_{1/6}Ti_{1/6}$ synthesized by spark plasma sintering. *Acta. Materialia.* **2022**, *232*, 117971. DOI
25. Martínez, E.; Mikheenko, P.; Martínez-lópez, M.; Millán, A.; Bevan, A.; Abell, J. S. Flux pinning force in bulk MgB_2 with variable grain size. *Phys. Rev. B.* **2007**, 75. DOI
26. Abou, E. H. A.; Labrag, A.; Taoufik, A.; et al. Magnetic penetration depth and coherence length in a single-crystal $YBa_2Cu_3O_{7-\delta}$. *Physica. Status. Solidi. (b).* **2021**, *258*, 2100292. DOI
27. Rowell, J. M. The widely variable resistivity of MgB_2 samples. *Supercond. Sci. Technol.* **2003**, *16*, R17-27. DOI
28. Jiang, J.; Senkowicz, B. J.; Larbalestier, D. C.; Hellstrom, E. E. Influence of boron powder purification on the connectivity of bulk MgB_2. *Supercond. Sci. Technol.* **2006**, *19*, L33-6. DOI
29. Muhammad, Y.; Rahim, M.; Hussain, N.; Iqbal, Z.; Naseem, A. Enhanced transport properties of $(Ag)_x$/CuTl-1223 nano-composites with the application of high pelletization pressure. *Appl. Phys. A.* **2024**, *130*, 7801. DOI
30. Matthews, G. A. B.; Mousavi, T.; Santra, S.; Grovenor, C. R. M.; Grant, P. S.; Speller, S. Improving the connectivity of MgB_2 bulk superconductors by a novel liquid phase sintering process. *Supercond. Sci. Technol.* **2022**, *35*, 065005. DOI
31. Xu, Z.; Jiang, Z.; Kuai, C.; et al. Charge distribution guided by grain crystallographic orientations in polycrystalline battery materials. *Nat. Commun.* **2020**, *11*, 83. DOI PubMed PMC
32. Wang, Q.; Zhao, C.; Hu, X.; et al. Grain-boundary-rich interphases for rechargeable batteries. *J. Am. Chem. Soc.* **2024**, *146*, 31778-87. DOI PubMed PMC
33. Son, D.; Lee, J.; Choi, Y. J.; et al. Self-formed grain boundary healing layer for highly efficient $CH_3NH_3PbI_3$ perovskite solar cells. *Nat. Energy.* **2016**, *1*, 16081. DOI
34. Sherkar, T. S.; Momblona, C.; Gil-Escrig, L.; et al. Recombination in perovskite solar cells: significance of grain boundaries, interface traps, and defect ions. *ACS. Energy. Lett.* **2017**, *2*, 1214-22. DOI PubMed PMC
35. Choi, H. H.; Paterson, A. F.; Fusella, M. A.; et al. Hall effect in polycrystalline organic semiconductors: the effect of grain boundaries. *Adv. Funct. Mater.* **2020**, *30*, 1903617. DOI
36. Sarkar, P.; Muhammed, A. A. V.; Ghorai, G.; et al. On the grain boundary charge transport in p-type polycrystalline nanoribbon transistors. *Nanoscale* **2024**, *16*, 16611-21. DOI
37. Wei, Z.; Wang, C.; Zhang, J.; et al. Precise regulation of carrier concentration in thermoelectric BiSbTe alloys via magnetic doping. *ACS. Appl. Mater. Interfaces.* **2020**, *12*, 20653-63. DOI
38. Kim, J. H.; Cho, H.; Back, S. Y.; Yun, J. H.; Lee, H. S.; Rhyee, J. Lattice distortion and anisotropic thermoelectric properties in hot-deformed CuI-doped $Bi_2Te_{2.7}Se_{0.3}$. *J. Alloys. . Compd.* **2020**, *815*, 152649. DOI
39. Kim, J. H.; Back, S. Y.; Yun, J. H.; Lee, H. S.; Rhyee, J. S. Scattering mechanisms and suppression of bipolar diffusion effect in $Bi_2Te_{2.85}Se_{0.15}I_x$ compounds. *Materials* **2021**, *14*, 1564. DOI PubMed PMC
40. Cao, T.; Shi, X.; Li, M.; et al. Advances in bismuth-telluride-based thermoelectric devices: progress and challenges. *eScience* **2023**, *3*, 100122. DOI
41. Hu, X.; Xiang, Q.; Kong, D.; et al. The effect of Ni/Sn doping on the thermoelectric properties of BiSbTe polycrystalline bulks. *J. Solid. State. Chem.* **2019**, *277*, 175-81. DOI

42. Zhu, T.; Gao, H.; Chen, Y.; Zhao, X. Ioffe-regel limit and lattice thermal conductivity reduction of high performance $(AgSbTe_2)_{15}(GeTe)_{85}$ thermoelectric materials. *J. Mater. Chem. A.* **2014**, *2*, 3251-6. DOI
43. Kim, H.; Kim, S. I.; Lee, K. H.; Kim, S. W.; Snyder, G. J. Phonon scattering by dislocations at grain boundaries in polycrystalline $Bi_{0.5}Sb_{1.5}Te_3$. *Physica. Status. Solidi. (b).* **2017**, *254*, 1600103. DOI
44. Bahk, J.; Shakouri, A. Minority carrier blocking to enhance the thermoelectric figure of merit in narrow-band-gap semiconductors. *Phys. Rev. B.* **2016**, *93*, 165209. DOI
45. Wei, Z.; Yang, Y.; Wang, C.; Li, Z.; Zheng, L.; Luo, J. Enhanced room-temperature thermoelectric performance of p-type BiSbTe by reducing carrier concentration. *RSC. Adv.* **2019**, *9*, 2252-7. DOI PubMed PMC
46. Cao, S.; Huang, Z. Y.; Zu, F. Q.; Xu, J.; Yang, L.; Chen, Z. G. Enhanced thermoelectric properties of Ag-modified $Bi_{0.5}Sb_{1.5}Te_3$ composites by a facile electroless plating method. *ACS. Appl. Mater. Interfaces.* **2017**, *9*, 36478-82. DOI
47. Dharmaiah, P.; Lee, K.; Song, S. H.; Kim, H. S.; Hong, S. Enhanced thermoelectric performance of $Bi_{0.5}Sb_{1.5}Te_3$ composites through potential barrier scattering at heterogeneous interfaces. *Mater. Res. Bull.* **2021**, *133*, 111023. DOI
48. Wu, G.; Yan, Z.; Wang, X.; et al. Optimized thermoelectric properties of $Bi_{0.48}Sb_{1.52}Te_3$ through AgCuTe doping for low-grade heat harvesting. *ACS. Appl. Mater. Interfaces.* **2021**, *13*, 57514-20. DOI
49. Li, Y.; Ren, M.; Sun, Z.; Yao, Z. Nanoarchitectonics of p-type BiSbTe with improved figure of merit via introducing PbTe nanoparticles. *RSC. Adv.* **2021**, *11*, 36636-43. DOI
50. Maksymuk, M.; Dzundza, B.; Matkivsky, O.; Horichok, I.; Shneck, R.; Dashevsky, Z. Development of the high performance thermoelectric unicouple based on Bi_2Te_3 compounds. *J. Power. Sources.* **2022**, *530*, 231301. DOI
51. Deng, R.; Su, X.; Hao, S.; et al. High thermoelectric performance in $Bi_{0.46}Sb_{1.54}Te_3$ nanostructured with ZnTe. *Energy. Environ. Sci.* **2018**, *11*, 1520-35. DOI